Article

4DOF Maneuvering Motion of a Container Ship in Shallow Water Based on CFD Approach

Tien Thua Nguyen *, Thanh Long Phan , Tat-Hien Le , Thi Loan Mai , Hyeon Kyu Yoon *

Article

4DOF Maneuvering Motion of a Container Ship in Shallow Water Based on CFD Approach

Tien Thua Nguyen [1], Thanh Long Phan [1], Tat-Hien Le [2], Thi Loan Mai [3] and Hyeon Kyu Yoon [3,*]

[1] The University of Danang-University of Science and Technology, Vietnam
[2] Ho Chi Minh City-University of Science and Technology-Vietnam National University (VNU-HCM), Vietnam
[3] Changwon National University, Republic of Korea
*   Correspondence: hkyoon@changwon.ac.kr

Abstract: With the continuous increase in ship size combined with the generally slower increase in the size of waterways, the need for the prediction of ship maneuvering in shallow waterways continues to attract attention from the international scientific community. Ship behavior in shallow water is relevant in seabed effects that result in changing the hydrodynamic forces acting on the ship. In this study, the maneuvering characteristics of container ship with four degrees of freedom in shallow water are analyzed. The Reynolds-averaged Navier Stokes approach in Ansys Fluent code is used to produce the maneuvering coefficients through the simulations of forward running, static drift, static heel, circular motion, the combined motions, and the pure roll motion of the Kriso container ship. The maneuvering characteristics of the ship are estimated for evaluating the ship behaviors in shallow water condition. The obtained results show that the roll has a significant decrease and the ship's turning diameter has a significant increase when the ship operates in the shallow waterway. The prediction of maneuvering characteristics of the ship are in good agreement with those of free running model tests, indicating that the numerical simulation based on the Computational Fluid Dynamics method has compromising capability to predict the maneuvering derivatives and the 4-DOF ship maneuvering motion in shallow water as well.

Keywords: container ship; hydrodynamic forces; four degrees of freedom; maneuvering characteristics; shallow water effects; CFD-based simulation

1. Introduction

A ship is designed for not only oceangoing transport but also moving in a restricted area. Maneuverability is one of the most important characteristics of the ship's performance that allows the ship to operate in safe and efficient conditions. Ship maneuverability in the open sea focuses on the navigation of ship journeys in calm water or in a random sea [1,4,5,12]. However, ship behavior in shallow water is associated with interaction between ship and the seabed that affect the dynamic behavior of the ship, changing its attitude and increasing risks [25]. Therefore, the International Maritime Organization (IMO) recommends that the maneuverability of a ship in shallow water should be included in the maneuvering booklet (IMO Resolution A.601, 1987) [17]. Previously, most studies addressed ship resistance and three degrees of freedom (3-DOF) maneuvering behavior in shallow water condition [4,5,8,9,19,21]. One of the first examples of the study of ship maneuvering in shallow water can be found in Gronarz [26] where the author performed the extended study of the hydrodynamics of the Panamax container ship in different water depths using the CFD-based simulation. The maneuvering derivatives of the ship in the shallow water case were represented as a function of the derivatives of the ship in deep water by using both the numeral results and experimental data. The results of the 3-DOF maneuvering simulation showed that the decrease in water depth resulted in the increase of turning radius and the decrease of the drift angle. Milanov and Chotukova carried out the experiments of Kriso Container Ship (KCS) in shallow water in the BSHC (Bulgarian Ship Hydrodynamics Centre) tank for three values of metacentric height [22]. It can be seen that the ship roll response to the rudder action in shallow water is much more moderate

compared with the deep-water case. Toxopeus performed the numerical study on the motion of KVLCC2 model to predict the variation of surge force, sway force and yaw moment for different water depths [24]. The calculated results show that the hydrodynamic forces acting on the hull in very shallow water have a non-linear form of sway velocity and yaw rate. Form factors also increase as the ship moves in shallow waters.

Delefortrie et.al. formulated the 6-DOF maneuvering model of KVLCC2 at water depth ratios of 1.2, 1.3, and 1.8 [18]. The hydrodynamic force and moment acting on the hull are mainly obtained from the captive model tests, where the ship is forced to move with three horizontal degrees of freedom accompanying free heave and pitch. Some numerical results of roll were introduced to the maneuvering model of the ship. It can be seen that the prediction of KVLCC2's maneuvering characteristics are in good agreement with those of the free-running tests. However, the prediction of roll was underestimated in comparision with the roll obtained from the Free Running Model Tests (FRMT). Additionally, Ruiz et. al. [23] studied the wave effects on the motion of the KVLCC2 model with 6-DOF in shallow water using both numerical and experimental methods. The experiment of 4-DOF KCS with rudder and propeller were conducted by Kim et. al. [6]. The captive model tests with Computerized Planar Motion Carriage were performed to estimate hydrodynamic coefficients, especially those related to roll. Hamid et. al. investigated the 4-DOF ONR tumblehome based on the CFD-generated maneuvering derivatives [20]. Then, maneuvering simulations were performed to evaluate the ship maneuvering behavior such as surge velocity, sway velocity, yaw rate, roll angle, heading angle, and the ship trajectory. CFD method was confirmed to have sufficient ability to predict the ship's maneuvering characteristics in calm water. The results also showed zigzag overshoot and under-prediction of the ship's turning diameter. Yasukawa and Hirata experimentally investigated the ship sailing in the heeled state [13]. The oblique towing and turning circle tests were performed on the container ship, pure car carrier, and the ferry to measure surge force, sway force, roll moment, and yaw moment. Hydrodynamic derivatives obtained from forces and moments were used to investigate course stability of the ship. It is proved that the course stability is deeply related to nonlinear derivatives of heel angle. Fukui [2] performed the circular motion test by setting a constant roll angle for a container ship and a passenger ferry in deep water. The effects of the roll angle on the hydrodynamic derivatives were extracted from the measured forces and moments. The suitable 4-DOF mathematical model was proposed to simulate the turning trajectories and the overshoot of the zigzag movement at several metacentric height values. It was concluded that maneuvering variables were well predicted by the mathematical model. Gu et. al. [3] also predicted hydrodynamic derivatives via the Reynolds-Averaged Navier Stokes (RANS) method to investigate the maneuvering of the 4-DOF tumblehome ship in deep water. The static heel angle, static drift, and the circular motion tests were performed to estimate the surge force, sway force, roll moment, and yaw moment. These forces and moments were approximated through Taylor series expansion to determine the maneuvering derivatives. The obtained result show that the derivatives are in good agreement with the experiment values except for the cross-coupled derivatives N'_{vvr}, Y'_ϕ, and K'_ϕ. The obtained derivatives were introduced into the 4-DOF MMG model to simulate the turning circle and zigzag tests. The outcome variables of the ship motion are well predicted in comparison with the FRMT results.

Although many studies have been conducted to investigate the effects of shallow water on ship maneuvering, little effort has been made on the 4-DOF maneuvering model of container ship in shallow water conditions. Therefore, this study addresses the prediction of maneuvering characteristics of the 4-DOF KCS model based on maneuvering derivatives that are generated by the CFD-based simulation.

2. Methodology

3.1. Maneuvering of the Container Ship with Four Degrees of Freedom

Normally, the 3-DOF model is considered in the maneuvering study of the surface ship; however, the roll of the thin hull such as the container ship is needed to be considered. To describe the ship maneuvering motion, two coordinate systems are considered: an earth-fixed coordinate system ($Ox_0y_0z_0$); and a body-fixed coordinate system ($Oxyz$). The coordinate systems follow the right-hand rule with the z-axes are pointing downward and the x-axes are pointing to the bow. The origin

of the body-fixed coordinate system is set at midship. The body-fixed coordinate system is moving the ship and it is used to express the linear velocities and angular velocities of the vehicle. The Earth-fixed reference is the inertial reference frame is adopted to represent the position and orientation of the ship. According to SNAME (The Society of Naval Architects and Marine Engineers), the position, orientation, and velocities of the ship motion in 4-DOF (Degrees Of Freedom) are described in the two coordinate systems as shown in Figure 1.
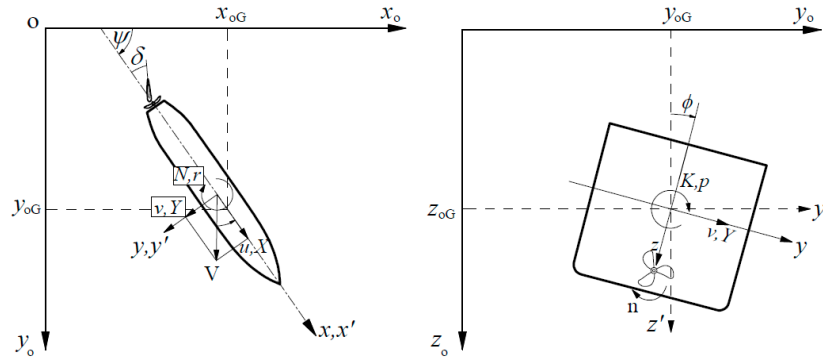

Figure 1. Coordinate systems and symbols.

The Son and Nomoto model for maneuvering motion in the surge, sway, roll, and yaw [15] is chosen to be the baseline of the KCS maneuvering study. The general form of the model is shown in Eq. (1). The hydrodynamic force model is shown in the following equations.

$$m[\dot{u} - vr - x_G r^2 + y_G \dot{r}] = X \tag{1}$$

$$m[\dot{v} + ur - y_G(r^2 + p^2) + x_G \dot{r}] = Y \tag{2}$$

$$I_x \dot{p} - I_{xz} \dot{r} + I_{yz} r^2 + I_{xy} pr + m[y_G vp - z_G(\dot{v} + ur)] = K \tag{3}$$

$$I_z \dot{r} - I_{yz} rp - I_{xy} p^2 - I_{zx} \dot{p} + m[x_G(\dot{v} + ur) - y_G(\dot{u} - vr)] = N \tag{4}$$

Regarding the ship motion in calm water, the external force and moment in the right side of the equations consist of hydrodynamic (F_H) and hydrostatic (F_S) forces acting on the hull, propeller forces (F_P) and rudder forces (F_R). The hydrodynamic force (X, Y) and moment (K, N) of the hull, rudder and the propeller are modeled as follows,

$$X' = X'_{uu} u'^2 + (1-t)T'(J) + X'_{vr} v'r' + X'_{vv} v'^2 + C'_{v\delta} v'\delta + X'_{rr} r'^2 + X'_{\phi\phi} \phi^2 + X'_{\delta\delta} \delta^2 \tag{5}$$

$$
\begin{aligned}
Y' = {} & Y'_v v' + Y'_r r' + Y'_p p' + Y'_\phi \phi + Y'_{v|v|} v' |v'| + Y'_{rrr} r'^3 + Y'_\delta \delta + Y'_{\delta\delta\delta} \delta^3 + Y'_{vvr} v'^2 + Y'_{vrr} v' r'^2 \\
& + Y'_{vv\phi} v'^2 \phi + Y'_{rr\phi} r'^2 \phi + Y'_{\phi\phi r} r' \phi^2
\end{aligned}
\tag{6}
$$

$$
\begin{aligned}
K' = {} & K'_v v' + K'_r r' + K'_p p' + K'_\phi \phi + K'_{vvv} v'^3 + K'_{rrr} r'^3 + K'_{vvr} v'^2 r' + K'_{rrv} r'^2 + K'_{vv\phi} v'^2 \phi + K'_{rr\phi} r'^2 + K'_{\phi\phi r} r' \phi^2 \\
& - (1 + a_H) z'_R Y_R \cos \delta
\end{aligned}
\tag{7}
$$

$$
\begin{aligned}
N' = {} & N'_v v' + N'_r r' + N'_p p' + N'_\phi \phi + N'_{v|v|} v' |v'| + N'_{rrr} r'^3 + N'_\delta \delta + N'_{\delta\delta\delta} \delta^3 + N'_{vvr} v'^2 r' + N'_{rrv} r'^2 v' \\
& + N'_{vv\phi} v'^2 \phi + N'_{rr\phi} r'^2 \phi + N'_{\phi\phi r} r' \phi^2 + N'_{vv\delta} v'^2 \delta + N'_{\delta\delta v} v' \delta^2
\end{aligned}
\tag{8}
$$

with (u', v') and (p', r') stand for the dimensionless linear velocities along x and y axes and rotational velocities about the x and z axes, respectively. The hydrodynamic coefficients are derived from dimensionless values of the hydrodynamic force and moment by ($\frac{1}{2}\rho L^2 U^2$) and ($\frac{1}{2} \rho L^3 U^2$).

3.2. Numerical Method

The fluid flow through the ship will be modeled using the Reynolds-averaged Navier Stokes (RANS) method. The governing equations [16,28] of the method for the incompressible flow over the ship can be expressed in the following equations,

$$\frac{\partial \overline{u}_i}{\partial x_i} = 0 \tag{9}$$

$$\frac{\partial \overline{u}_i}{\partial t} + \overline{u}_j \frac{\partial \overline{u}_i}{\partial x_j} = -\frac{\partial \overline{p}}{\partial x_i} + v \frac{\partial^2 \overline{u}_i}{\partial x_j \partial x_j} + g - \frac{\partial \tau_{ij}}{\partial x_j} \tag{10}$$

The Reynolds stress, $\tau_{ij} = \overline{u_i' u_j'}$, is modeled with the function of eddy viscosity and kinetic energy based on the Boussinesq hypothesis. The turbulent model, k-ω SST (Shear Stress Transport) [7,11,14,16,33] for solving turbulent flow around the submarine is presented as following:

$$\frac{\partial k}{\partial t} + \overline{u}_i \frac{\partial k}{\partial x_i} = P_k - \beta^* \omega k + \frac{\partial}{\partial x_j}\left((v + \sigma_k v_t)\frac{\partial k}{\partial x_i}\right) \tag{11}$$

$$\frac{\partial \omega}{\partial t} + \overline{u}_i \frac{\partial \omega}{\partial x_i} = \frac{\gamma}{\mu_t} P_k - \beta \omega^2 + \frac{\partial}{\partial x_j}\left[(v + \sigma_\omega v_t)\frac{\partial \omega}{\partial x_i}\right] + 2(1 - F_1)\frac{\sigma_{\omega 2}}{\omega}\frac{\partial k}{\partial x_i}\frac{\partial \omega}{\partial x_i} \tag{12}$$

$$\mu_t = \frac{\rho a_1 k}{max(a_1 \omega, \Omega F_2)} \tag{13}$$

with the variables are defined as follows,

$$P_k = \tau_{ij}\frac{\partial u_i}{\partial x_j}$$

$$\tau_{ij} = \mu_t \left(2S_{ij} - \frac{2}{3}\frac{\partial u_k}{\partial x_k}\delta_{ij}\right) - \frac{2}{3}\rho k \delta_{ij}$$

$$S_{ij} = \frac{1}{2}\left(\frac{\partial u_i}{\partial x_j} + \frac{\partial u_j}{\partial x_i}\right)$$

$$\beta_i = F_1 \beta_{i,1} + (1 - F_1)\beta_{i,2}$$

$$\sigma_k = \frac{1}{F_1/\sigma_{k,1} + (1 - F_1)\sigma_{k,2}}$$

$$\sigma_\omega = \frac{1}{F_1/\sigma_{\omega,1} + (1 - F_1)\sigma_{\omega,2}}$$

$$F_1 = \tanh\left(arg_1^4\right)$$

$$F_2 = \tanh\left(arg_2^2\right)$$

$$arg_1 = min\left[max\left(\frac{\sqrt{k}}{\beta^* \omega y}; \frac{500v}{y^2 \omega}\right), \frac{4\rho \sigma_{\omega_2} k}{CD_{k\omega} y^2}\right]$$

$$arg_2 = max\left(2\frac{\sqrt{k}}{0.09\omega y}; \frac{500v}{y^2 \omega}\right)$$

$$CD_{k\omega} = max\left(2\rho \sigma_{\omega,2}\frac{1}{\omega}\frac{\partial k}{\partial x_i}\frac{\partial \omega}{\partial x_i}, 10^{-20}\right)$$

with the model constants are: $\sigma_{k,1}$=1.176, $\sigma_{\omega,1}$=2.0, $\sigma_{k,2}$=1.0, $\sigma_{\omega,2}$=1.168, a_1=0.31, $\beta_{i,1}$=0.075, $\beta_{i,2}$=0.0828.

The variation of free water surface [32] are calculated from the fomulation of VOF (Volume of Fluid) in which the volume fraction (α_q) will be 0 or 1 for the cell with emty of water or full of water, correspondingly. The cell contains both water and air phases if the volume fraction is between 0 and 1. Continuity equation for the volume fraction of the phases, volume fraction of the primary phase and implicit scheme for calculating the face fluxes for all cells are presented in the following equations, respectively.

$$\frac{1}{\rho_q}\left[\frac{\partial}{\partial t}(\alpha_q\rho_q) + \nabla(\alpha_q\rho_q\vec{v}_q) = S_{\alpha_q} + \sum_{p=1}^{n}(\dot{m}_{pq} - \dot{m}_{qp})\right] \tag{14}$$

$$\sum_{q=1}^{n}\alpha_q = 1 \tag{15}$$

$$\frac{\alpha_q^{n+1}\rho_q^{n+1} - \alpha_q^{n}\rho_q^{n}}{\Delta t}V + \sum_{f}(\rho_q^{n+1}U_f^{n+1}\alpha_{q,f}^{n+1}) = \left[S_{\alpha_q} + \sum_{p=1}^{n}(\dot{m}_{pq} - \dot{m}_{qp})\right]V \tag{16}$$

where indexes (n, $n+1$) stand for previous time step and current time step. $\alpha_{q,f}$ is the face value of the qth volume fraction. V is the volume of cell and U_f is volume flux through the face. $\dot{m}_{pq}$ *and* $\dot{m}_{qp}$ is the masses transfer from phase q to phase p and vice versa. S_{α_q} is the source term.

3. Numerical Study

3.1. KCS Ship Model and Simulation Setup

The candidate ship presented in this study is KRISO Container Ship (KCS) with a bulbous bow and transom. The ship is equipped with a fixed-pitch five-blade propeller and a semi-balance horn rudder as shown in Figure 2. As mentioned in SIMMAN2020 [34], the full-scaled KCS is assumed to be operated at a speed of 8.75 knots in shallow water area without considering the bank effects. Thus, a corresponding scaled model with the length between perpendiculars of 1.5 meters is used and a flat sea bottom is specified in this numerical study. The stationary straight-line motions, circular motions, the combined motions, and the pure roll are simulated for predicting the maneuvering derivatives of the 4-DOF model of KCS ship at water depth ratios of 1.5 and 2.0. The main particulars of the hull, propeller, and rudder are tabulated in Table 1. The constraints of the tests are shown in Table 2.
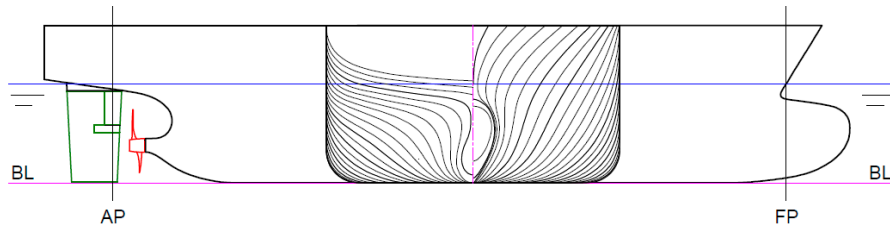

Figure 2. KCS model and appendages.

Table 1. Main particulars of KCS and appendages.

Designation	Unit	Full scale	Model scale
L_{pp}	m	230.0	1.500
B_{wl}	m	32.20	0.210
H	m	19.0	0.124
T	m	10.8	0.070
CB	-	0.651	0.651
∇	m³	52030	0.0144
LCB	%, fwd+	-1.48	-1.48

LCG	m	111.6	0.728
KG	m	14.32	0.0934
k_{xx}/B	-	0.400	0.400
k_{zz}/L_{PP}	-	0.250	0.250
GM_T	m	0.600	0.0039

Table 2. Test conditions for forward, drift, heal, and circular motion and combined motion.

Case	V (knots)	β (degree)	ϕ (degree)	r' [-]
Straight forward	7, 8.75, 10, 12	0	0	0
Static drift	8.75	4, 8, 12, 16	0	0
Static heel	8.75	0	0, 2, 4, 6, 8, 10	0
Circular motion	8.75	0	0	0.3, 0.35, 0.40, 0.50
Combined drift-heel	8.75	4, 6, 8, 12	2, 4, 8	0
Combined heel-CMT	8.75	0	2, 4, 6	0.3, 0.4, 0.5
Combined drift-CMT	8.75	4, 6, 8, 12	0	0.3, 0.4, 0.5

Table 2. Test conditions of the harmonic roll.

ϕ_{max} [degree]	ω (rad/s)	p (rad/s)	$\dot{p}$ (rad/s^2)
5	0.6	5.236×10^{-2}	-3.141×10^{-2}
5	0.8	6.981×10^{-2}	-5.585×10^{-2}
5	1.0	8.726×10^{-2}	-8.726×10^{-2}

In this study, the hydrodynamic forces acting on the ship are the main concern for estimating the maneuvering derivatives. The results of the CFD-based simulation are verified with the experimental results from KRISO [34] and Gronaz [26]. Straight-line tests, circular tests, and combined tests are numerically simulated using the RANS-based method for incompressible flow. The fluid domains are chosen to avoid the influence of boundary conditions such as inlet, outlet, and side walls. The rectangular domain has opted for the stationary straight-line tests and the harmonic tests. For the stationary straight-line tests, the domain is divided into two parts, the inner part and outer part, and the fluid flow over the ship is simulated in the stationary reference frame. On the other hand, the circular domain is used to simulate the steady circular tests in the rotating reference frame. According to International Towing Tank Conference (ITTC) Recommendation on Practical Guidelines for Ship CFD Application [30], the boundaries should be located 1.0~2.0L_{PP} away from the hull. In addition, the domain size must be increased in cases of ship simulation with the free surface condition. Therefore, the dimensions of the rectangular domain are chosen to be 6.5L_{PP} in length, 4.0L_{PP} in width, and 1.0L_{PP} in height. The inner radius, outer radius, and thickness of the circular domains are 0.2L_{PP}, 5.0L_{PP}, and 0.6L_{PP}. In addition, physical conditions will be applied to the boundary of the domain. The front and back sides of the rectangular domain are assigned corresponding pressure inlet and pressure outlet. The slip condition is set for the side walls and the no-slip condition is specified for hull surfaces and sea-bottom. The top face of the domain is considered as the symmetry conditions. For the circular domain, the front face and outer surface are assigned to the velocity inlet condition. The pressure outlet condition is set for the back face. The ship hull and bottom face are considered the no-slip conditions. Figures 3~4 show the typical domains and their dimensions for the straight-line and oblique tests, 2D pure roll, and circular tests, respectively.
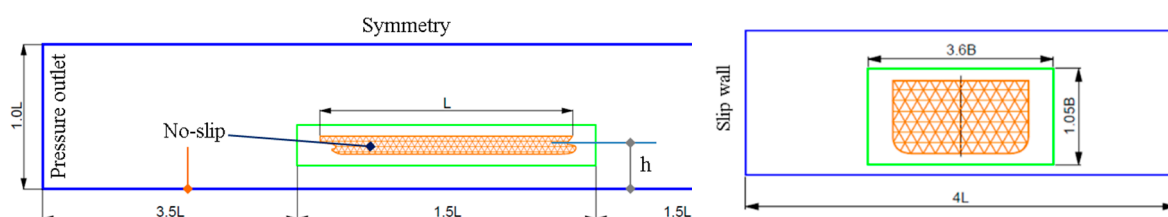
(**a**) Front view   (**b**) Side view

Figure 3. The fluid domain for straight-line motion and oblique motion

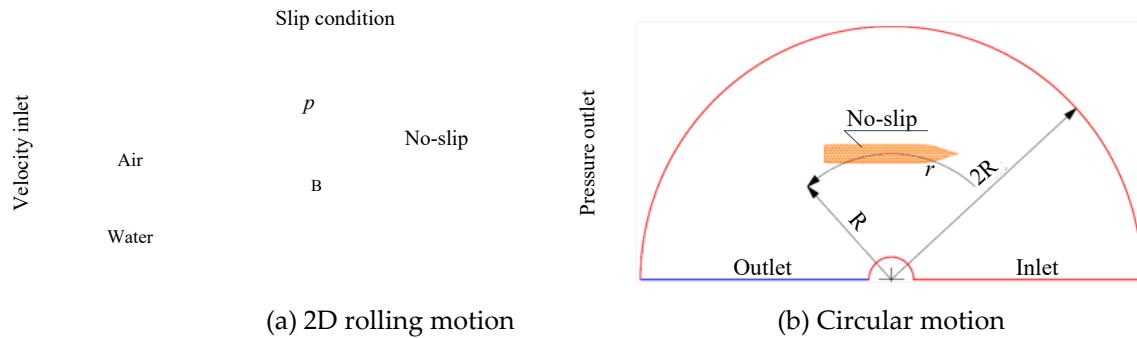(a) 2D rolling motion   (b) Circular motion

Figure 4. Fluid domain for 2D rolling motion and circular motion

3.2. Mesh Independant Study

Grid generation is the following step for discretizing the fluid domain into a number of control volumes. The hybrid mesh is adopted for the stationary straight-line tests oblique towing tests. The unstructured mesh is more flexible to facilitate the mesh generation of complex geometry and it, therefore, is used to discretize the inner domain including the hull. Specifically, the boundary layer domain is discretized using a prism mesh grown out of triangle mesh on the hull surface for resolving the viscous flow surrounding the hull. The tetrahedral mesh is used elsewhere away from the hull. The height of the first prism layer next to the ship wall is calculated for satisfying the y^+ value of 10, corresponding to the transition flow regime at the Reynolds number of 5.4×10^5. On the other hand, the outer part is discretized using the structured mesh that can help to reduce the grid size. Hexahedral elements are applied to the outer domain. The typical meshes of the oblique motion and the circular motion are illustrated in Figures 3~4, respectively. The number of elements in the corresponding meshes is approximate 5.6 million and 3.4 million. The maximum skewness of the meshes is kept smaller than 0.84. The RANS-based solver in ANSYS Fluent code is chosen as a tool for simulating the fluid flow through the hull. According to the ITTC Practical Guidelines for Ship CFD Application [30], the two-equation turbulence models have shown to be able to give an accurate prediction of the ship hydrodynamic. Thus, the k-ω SST turbulence model is opted for modeling turbulent flow around the hull. SIMPLE (Semi-implicit method for pressure link equations) algorithm is employed to solve the governing equations iteratively. The least-square cell-based method is used for evaluating the gradient of flow variables. The quantities at cell faces are calculated from the cell-centered values by using the second-order upwind method.

For the concerned geometry, a series of grids are generated and the CFD computations are performed. The variation in the results of the CFD computation are then analyzed. Grid Convergence Index (GCI) method [29] is applied to evaluate the variation and the mesh discretization error. According to this method, at least three levels of grids – coarse, medium, and fine are generated. The grid convergence parameters for the fine mesh (1), medium mesh (2), and coarse mesh (3) are defined as follows,

- Grid convergence rate:

$$p = \frac{\ln\left(\frac{\varepsilon_{32}}{\varepsilon_{21}}\right)}{\ln(r_G)} \tag{17}$$

- Grid convergence ratio:

$$R_G = \frac{\varepsilon_{21}}{\varepsilon_{32}} \tag{18}$$

- Grid convergence index:

$$GCI_{ij} = F_S \frac{|e_{ij}|}{r^p - 1} \qquad (19)$$

where $\varepsilon_{ij} = \phi_j - \phi_i$, $e_{ij} = (\phi_j - \phi_i)/\phi_j$, and ϕ_i denotes the solution on the ith grid. F_s is 1.5 for the study with unstructured mesh.

GCI (Grid Convergence Index) method is applied to investigate the discretization error for the three meshes: fine mesh (1), medium mesh (2), and coarse mesh (3). The cases of static drift test at β=12º and combined drift-heel test at β=12º and ϕ=8º are chosen to examine the discretization errors. The generated mesh sizes for the static drift test are 1978999 nodes, 2638389 nodes, and 2794898 nodes, corresponding to the coarse grid, medium grid, and fine grid while these are 2433339 nodes, 2561101 nodes, and 2873365 nodes for the combined test case. The slices of the three mesh for these cases are shown in Figure 5. Table 4 shows the hydrodynamic forces and moments with respect to the three meshes. It is visible that the errors of the solutions are decreased when the meshes are generated more finely. According to Table 5, the numerical uncertainties of the X, Y, and N obtained from the static drift test for the coarse mesh, medium mesh and fine mesh are 7.76%, 4.62%, and 2.22%, respectively. Similarly, the numerical uncertainties for the mesh cases of the combined drift-heel test are 6.56%, 1.72%, 2.18%, and 0.85% for X, Y, K, and N, respectively. These quantities indicate that the solutions of Y, K, and N of the fine mesh are independency of grid generation while the X force has a small change when the mesh quality is varied. From the grid-independent study, the fine mesh is chosen for the entire CFD-based simulations in this study.
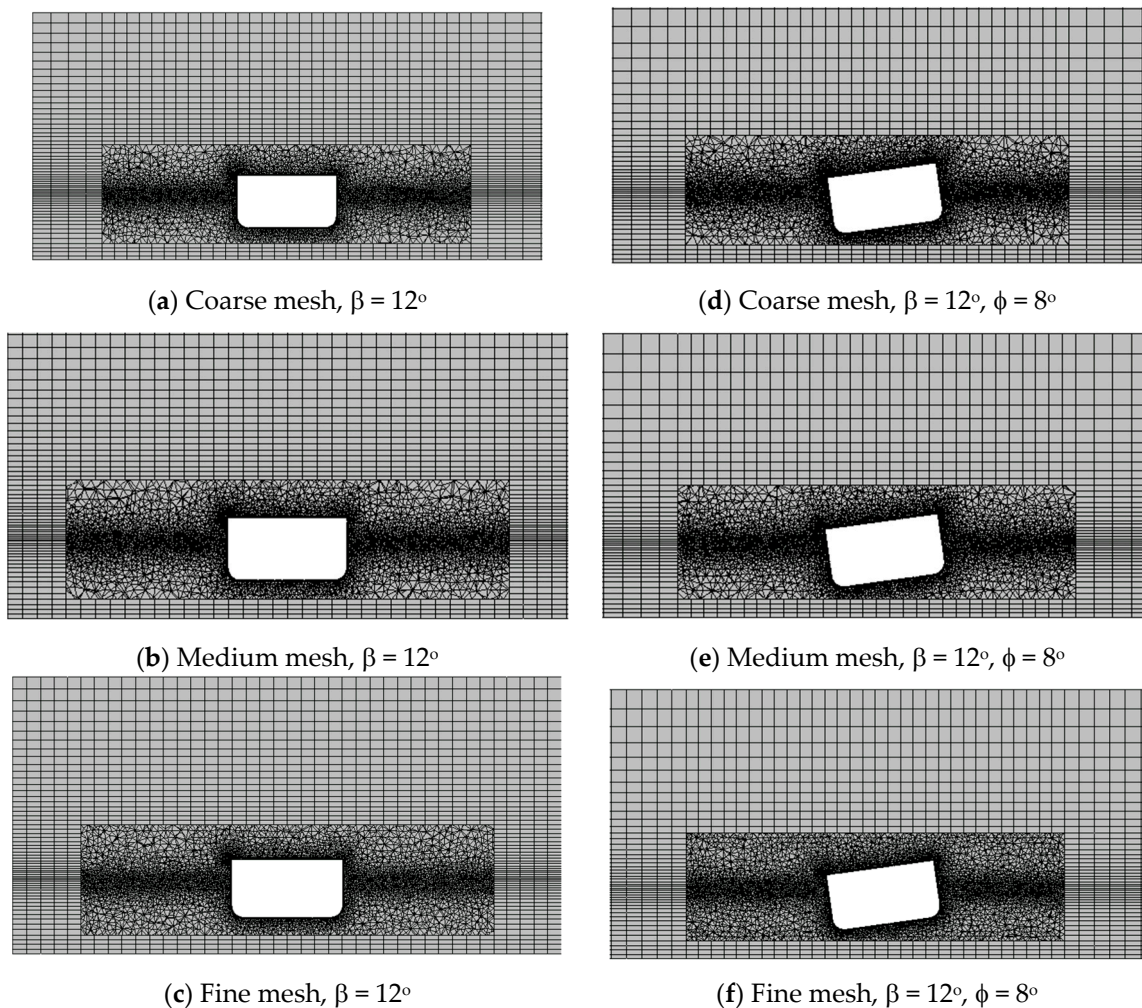

(**a**) Coarse mesh, β = 12º

(**d**) Coarse mesh, β = 12º, ϕ = 8º

(**b**) Medium mesh, β = 12º

(**e**) Medium mesh, β = 12º, ϕ = 8º

(**c**) Fine mesh, β = 12º

(**f**) Fine mesh, β = 12º, ϕ = 8º

Figure 5. Mesh sizes for static drift test (left) and combined drift-heel test (right), h/T=2.0

Table 4. Hydrodynamic forces and moments in static drift test and drift-heel test, h/T=2.0.

Mesh size	Static drift test, β=12º			Combined drift-heel test, β=12º, φ=8º			
	X [N]	Y [N]	N [N.m]	X [N]	Y [N]	K [N.m]	N [N.m]
Coarse	-0.199	-0.760	-0.320	-1.39×10^{-3}	-3.31×10^{-3}	1.71×10^{-3}	1.83×10^{-3}
Medium	-0.202	-0.778	-0.327	-1.44×10^{-3}	-3.46×10^{-3}	1.75×10^{-3}	1.85×10^{-3}
Fine	-0.204	-0.789	-0.330	-1.47×10^{-3}	-3.5×10^{-3}	1.77×10^{-3}	1.85×10^{-3}

Table 5. Grid convergence study.

	Static drift test, β=12º			Combined drift-heel test, β=12º, φ=8º			
	X	Y	N	X	Y	K	N
ε_{32}	-2.02×10^{-5}	-1.26×10^{-4}	-2.94×10^{-5}	-5.03×10^{-5}	-1.49×10^{-4}	3.79×10^{-5}	1.93×10^{-5}
ε_{21}	-1.50×10^{-5}	-7.20×10^{-5}	-1.39×10^{-5}	-3.14×10^{-5}	-7.57×10^{-5}	1.71×10^{-5}	8.01×10^{-6}
ε_{32}	1.46×10^{-2}	2.35×10^{-2}	1.96×10^{-2}	3.50×10^{-2}	4.30×10^{-2}	2.17×10^{-2}	1.05×10^{-2}
ε_{21}	1.07×10^{-2}	1.33×10^{-2}	9.19×10^{-3}	2.14×10^{-3}	2.14×10^{-2}	9.71×10^{-3}	4.32×10^{-3}
p_G	8.45×10^{-1}	1.61	2.17	1.35	1.95	2.29	2.54
R_G	0.746	0.573	0.472	0.625	0.509	0.452	0.415
GCI_{fine}	7.76%	4.62%	2.22%	6.56%	1.72%	2.18%	0.85%

4. Results

4.1. Hydrodynamic Forces and Moments Acting on the KCS Model

Figures 6~15 show the computation results of hydrodynamic forces and moments of the straight-line tests at water depth ratios of 1.5 and 2.0. In general, the overall trend shows that the hydrodynamic forces and moments are augmented when the water depth level is decreased. The roll moment linearly increases with the increase of the roll angle while the other forces moments have nonlinear variation with respect to the motion constraints. The similar trends for the results of the steady circular tests and the combined heel-CMT and combined drift-heel tests are shown in Figure 8 and Figures 10~15. The relationship between the surge force, sway force, and yaw moment with respect to yaw rate is nonlinear. These forces and moments increase with the increase of the yaw rate.
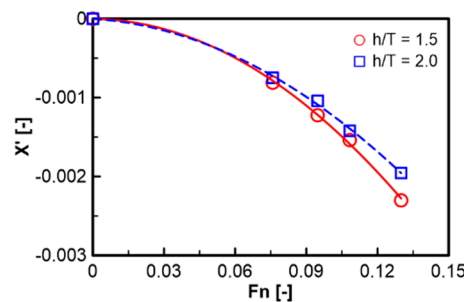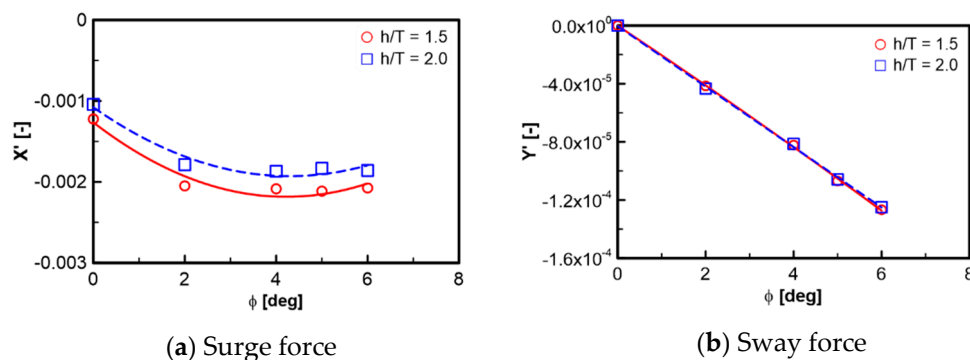

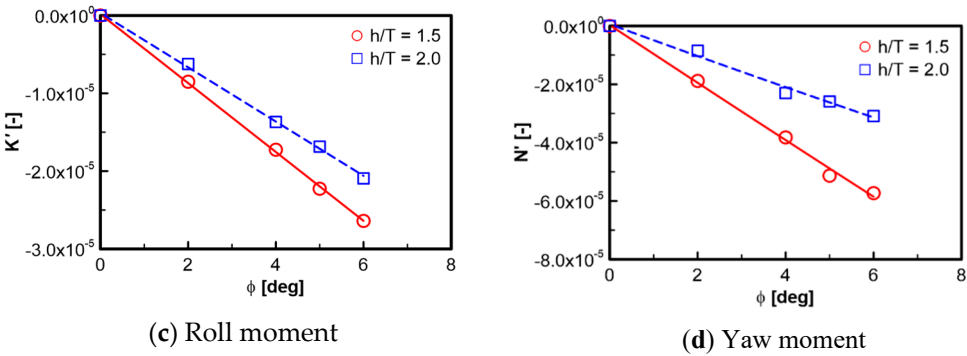**Figure 6.** Forward running test.

(**a**) Surge force	(**b**) Sway force

(**c**) Roll moment

(**d**) Yaw moment

Figure 7. Static heel test

(**a**) Surge force versus yaw rate

(**b**) Sway force versus yaw rate
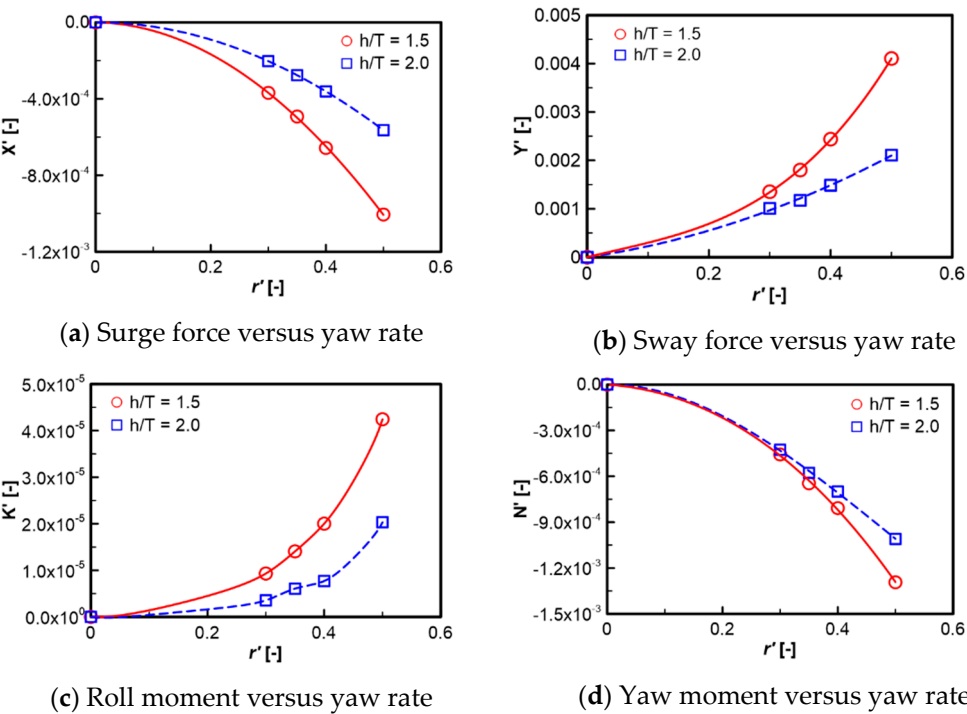

(**c**) Roll moment versus yaw rate

(**d**) Yaw moment versus yaw rate

Figure 8. Circular motion test

(**a**) Surge force versus drift angle

(**b**) Sway force versus drift angle

(**c**) Yaw moment versus drift angle
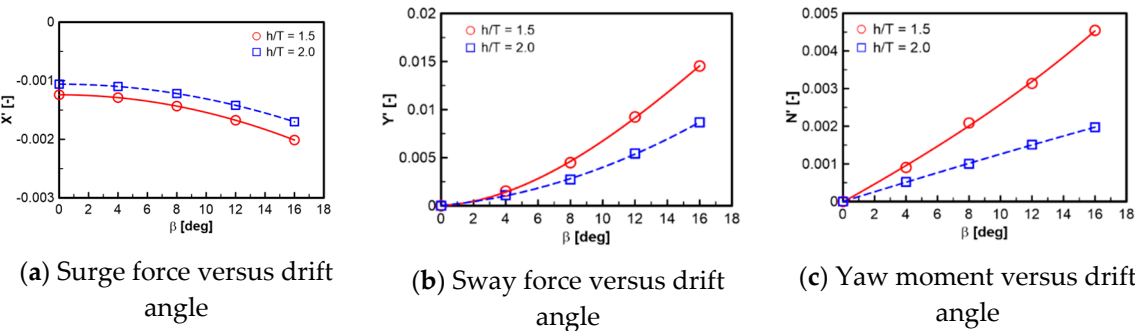
Figure 9. Static drift test

(**a**) Sway force   (**b**) Roll moment   (**c**) Yaw moment
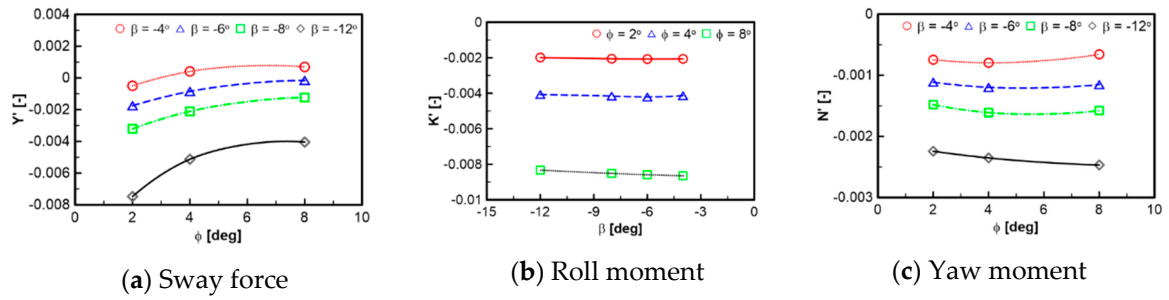
Figure 10. Combined heel-drift test, h/T = 1.5.

(**a**) Sway force   (**b**) Roll moment   (**c**) Yaw moment
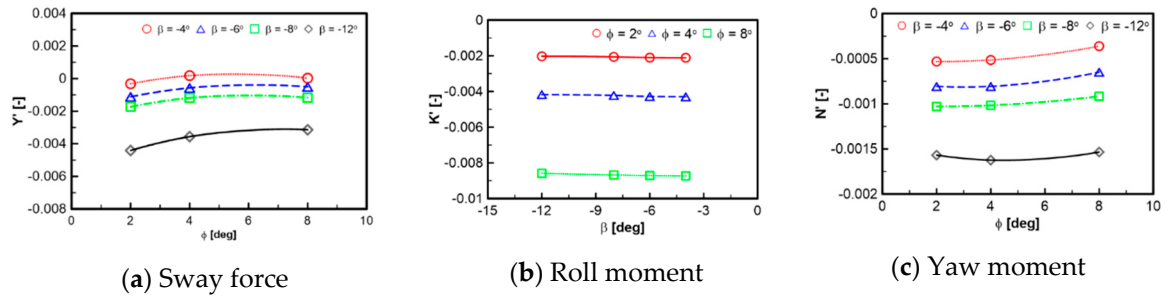
Figure 11. Combined heel-drift test, h/T = 2.0.

(**a**) Surge force   (**b**) Sway force   (**c**) Yaw moment
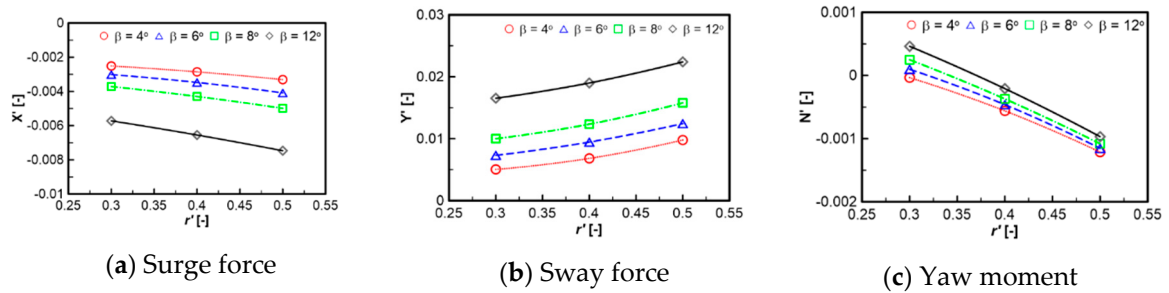
Figure 12. Combined drift-CMT test, h/T = 1.5.

(**a**) Surge force   (**b**) Sway force   (**c**) Yaw moment
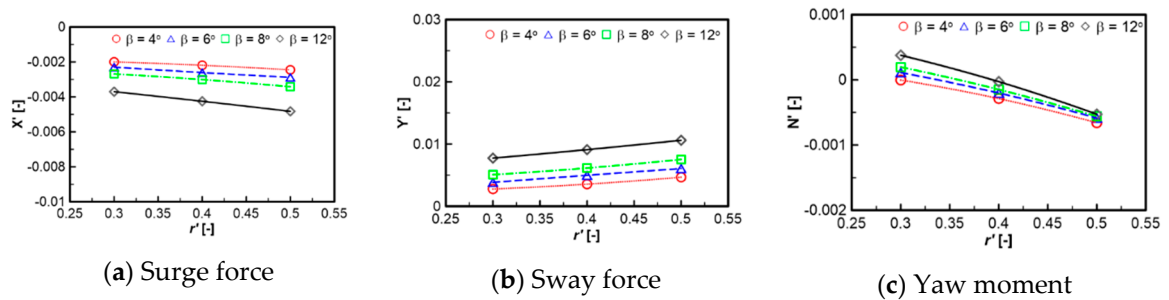
Figure 13. Combined drift-CMT test, h/T = 2.0.

(**a**) Surge force   (**b**) Sway force   (**c**) Yaw moment
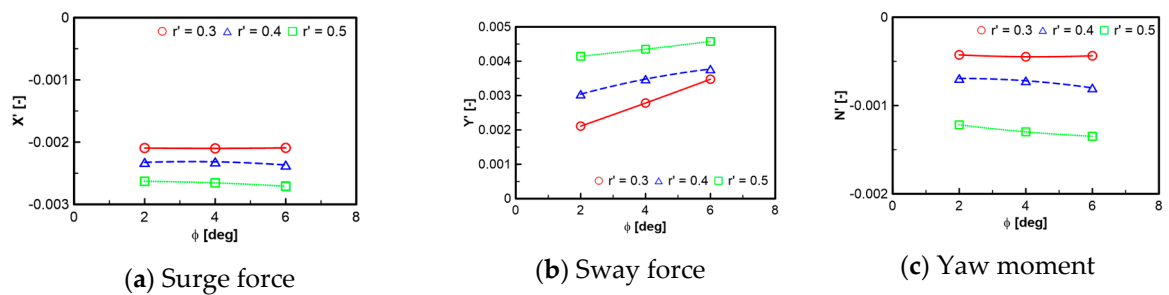
Figure 14. Combined heel-CMT test, h/T = 1.5.

(**a**) Surge force　　　　　(**b**) Sway force　　　　　(**c**) Yaw moment
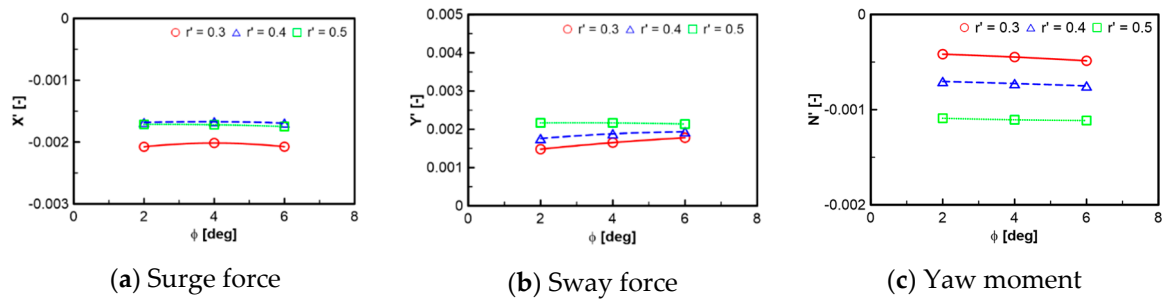
Figure 15. Combined heel-CMT test, h/T = 2.0.

For the harmonic motions, pure roll tests of the midship section are carried out. Fourier's analysis is applied to analyze the resulting roll moment to derive the in-phase and out-phase components. The roll moment of the ship is obtained by integrating the roll moment of the section over the length of the ship. Figure 16 shows the in phase and out phase components of the roll moment for the midship section of the KCS. Added roll moment and roll damping are estimated by linear approximation of the in-phase component and out-phase component, respectively.

(**a**) In-phase component

(**b**) Out-phase component
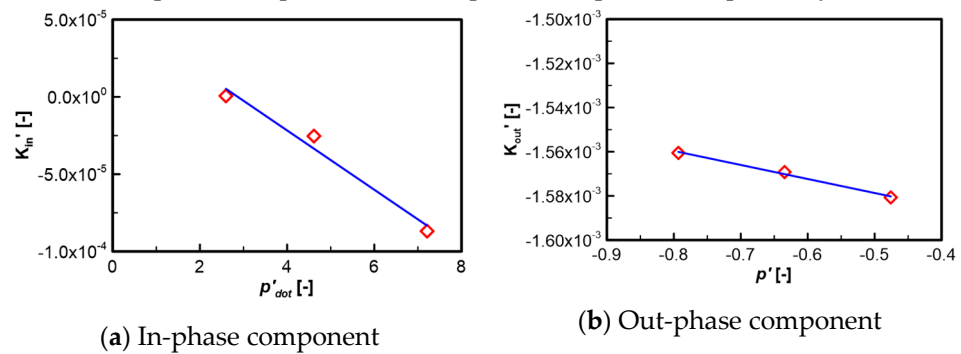
Figure 16. Results of 2D pure roll test, h/T = 2.0.

4.2. Verification Study

The maneuvering derivatives determined from the current CFD analysis of the KCS in shallow water are verified with the derivatives obtained from experimental results of KRISO from SIMMAN2020 [34], the experimental work by Gronarz [26]. From the comparison shown in Figures 17~20, it is clear to note that the sway force and yaw moment obtained from the static drift tests are in good agreement with those experimental results from the abovementioned researchers. On the other hand, there is a large discrepancy in surge force between the CFD results and the experimental results of KRISO and some discrepancy in sway velocity-dependent of surge force between the CFD result and the experimental data in [26] can be found. Thus, the differences between the current CFD results and the KRISO experimental results might be stem from the interaction between the hull, propeller, and rudder. The sway-velocity dependent derivatives of sway forces and yaw moments are in good agreement with the experimental results of KRISO. However, the nonlinear derivatives of yaw moment obtained from the KRISO experiment are greater than the derivatives determined from the current CFD computation. On the contrary, the rotary derivatives obtained from Gronaz's experiments are rather small in comparison with current CFD results. It is curious that the current CFD study gives a rotary derivative of sway force that is greater than the rotary derivative of yaw moment but the opposite trend is found in the results of Gronaz. The comparison of rotary derivatives and the cross-coupled derivatives are depicted in Figure 19.
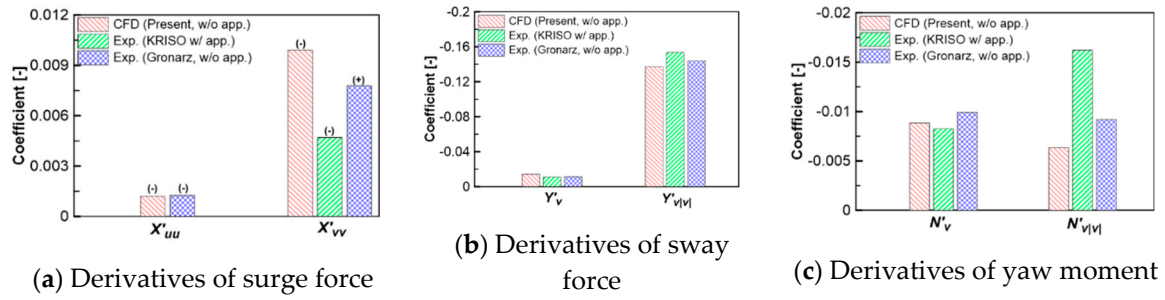
(**a**) Derivatives of surge force

(**b**) Derivatives of sway force

(**c**) Derivatives of yaw moment

Figure 17. Comparison of velocity-dependent derivatives of surge force, sway force, and yaw moment, h/T = 1.5.

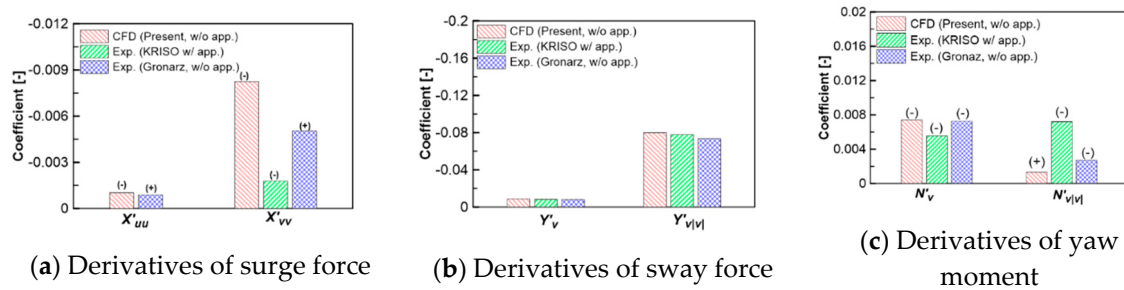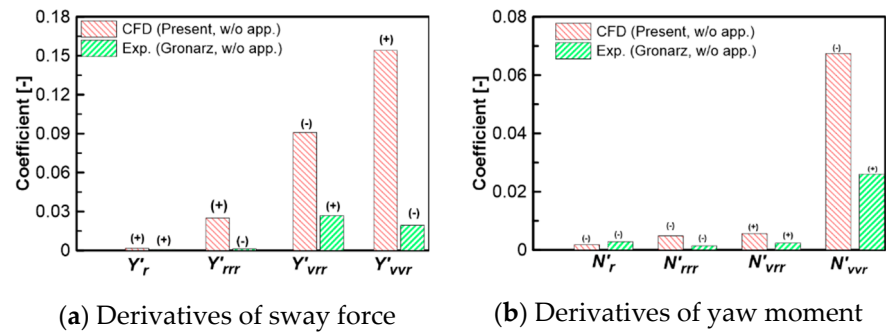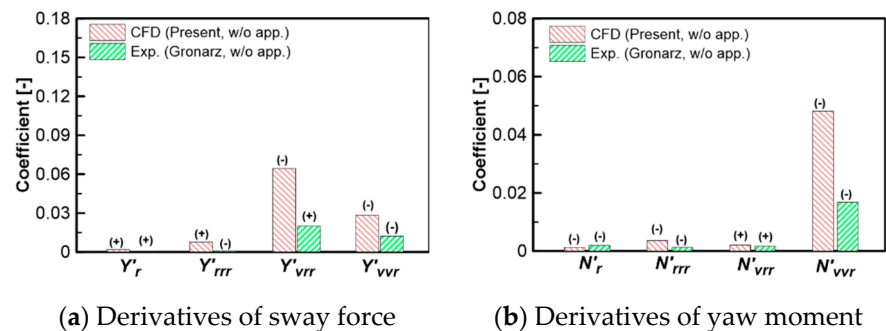(**a**) Derivatives of surge force

(**b**) Derivatives of sway force

(**c**) Derivatives of yaw moment

Figure 18. Comparison of velocity-dependent derivatives of surge force, sway force, and yaw moment, h/T = 2.0.

(**a**) Derivatives of sway force

(**b**) Derivatives of yaw moment

Figure 19. Comparison of velocity-dependent derivatives of surge force, sway force, and yaw moment, h/T = 1.5.

(**a**) Derivatives of sway force

(**b**) Derivatives of yaw moment

Figure 20. Comparison of velocity-dependent derivatives of surge force, sway force, and yaw moment, h/T = 2.0.

4.3. Maneuvering Simulation

The obtained maneuvering derivatives of the surge force, sway force, roll moment, and yaw moment are tabulated in Tables 6~7 for the water depth ratios of 1.5 and 2.0, respectively. It is noticed

that the surge, sway, and yaw inertia terms are taken from Mucha [27]. The parameters of the ship, propeller, and rudder are taken from SIMMAN 2020 [34]. The vertical center of gravity of the model is taken from the research of Tezdogan [10]. For evaluating the KCS maneuvering in shallow water, standard maneuvering simulations are performed at a speed of 8.75 knots for the cases of a water depth ratio of 1.5 and 2.0. The results from this maneuvering study are then compared with the results of free-running model tests involving the hard rudder turning maneuvers at δ_R = -35° [22].

Table 6. Non-dimensional maneuvering derivatives of KCS model ($\times 10^3$), h/T = 1.5.

X- coefficients	Y-coefficient	K-coefficient	N-coefficient
X'_{uu} = -1.206	Y'_v = -14.425	K'_ϕ = -0.251	N'_v = -8.829
X'_{vv} = -9.909	$Y'_{v\|v\|}$ = -137.059	K'_v = -0.221	$N'_{v\|v\|}$ = -6.325
$X'_{\phi\phi}$ = -4.348	$Y'_{r.}$ = 1.539	K'_{vvv} = 21.571	N'_r = -1.783
X'_{rr} = -4.022	Y'_{rrr} = 25.05	K'_r = -0.0651	N'_{rrr} = -4.805
X'_{vr} = 51.498	Y'_{vrr} = -90.860	K'_{rrr} = 0.4687	N'_{vrr} = 5.464
$X'_{\delta\delta}$ = -2.223	Y'_{vvr} = 15.979		N'_{vvr} = -66.939
$X'_{v\delta}$ = -8.970	Y'_ϕ = -1.214		N'_ϕ = -0.561
	$Y'_{\phi vv}$ = 238.265		$N'_{vv\phi}$ = -108.258
	$Y'_{v\|\phi\|}$ = 107.489		$N'_{v\|\phi\|}$ = 13.926
	$Y'_{\phi rr}$ = -298.522		$N'_{\phi rr}$ = -5.052
	$Y'_{r\|\phi\|}$ = 157.118		$N'_{r\|\phi\|}$ = 0.742
	Y'_δ = 5.652		N'_δ = -2.304
	$Y'_{\delta\delta\delta}$ = -5.522		$N'_{\delta\delta\delta}$ = 11.496
	$Y'_{vv\delta}$ = 44.616		$N'_{vv\delta}$ = 1.496
	$Y'_{v\delta\delta}$ = 1759.4		$N'_{v\delta\delta}$ = 787.52

**Table 7.** Non-dimensional maneuvering derivatives of KCS model ($\times 10^3$), h/T = 2.0.

X- coefficients	Y-coefficient	K-coefficient	N-coefficient
$X_{\dot{u}}$ = -0.417	$Y_{\dot{v}}$ = -8.573	$K_{\dot{p}}$ = -0.0193	$N_{\dot{r}}$ = -1.242
X'_{uu} = -1.107	$Y_{\dot{r}}$ = 0.0414	K'_p = -0.0635	$N_{\dot{v}}$ = 0.217
X'_{vv} = -8.246	Y'_v = -8.685	K'_ϕ = -0.200	N'_v = -7.433
$X'_{\phi\phi}$ = -0.391	$Y'_{v\|v\|}$ = -79.797	K'_v = 0.711	$N'_{v\|v\|}$ = 1.334
X'_{rr} = -2.257	Y'_r = 1.830	K'_{vvv} = 2.485	N'_r = -2.385
X'_{vr} = 27.417	Y'_{rrr} = 7.673	K'_r = -0.071	N'_{rrr} = -1.026
$X'_{\delta\delta}$ = -2.668	Y'_{vrr} = -64.647	K'_{rrr} = 0.312	N'_{vrr} = 0.372
$X'_{v\delta}$ = -3.747	Y'_{vvr} = -28.413		N'_{vvr} = -44.538
	Y'_ϕ = -1.180		N'_ϕ = -0.619
	$Y'_{\phi vv}$ = 87.101		$N'_{vv\phi}$ = -156.10
	$Y'_{v\|\phi\|}$ = 39.321		$N'_{v\|\phi\|}$ = 36.530
	$Y'_{\phi rr}$ = -125.100		$N'_{\phi rr}$ = -10.481
	$Y'_{r/\phi/}$ = 60.300		$N'_{r\|\phi\|}$ = 4.318
	Y'_δ = -5.459		N'_δ = 2.428
	$Y'_{\delta\delta\delta}$ = 5.258		$N'_{\delta\delta\delta}$ = -1.916
	$Y'_{vv\delta}$ = -64.981		$N'_{vv\delta}$ = 38.004
	$Y'_{v\delta\delta}$ = 762.950		$N'_{v\delta\delta}$ = 322.200

The standard maneuvers are simulated for evaluating the ship maneuvering characteristics in shallow water conditions. The equation of motion is established after introducing the hydrodynamic forces, the rudder forces, and the propeller forces. The equation is then numerically solved by using the Microsoft Visual C++ 10 Express. The fourth order Runge-Kutta method is employed to find the approximate values of the ship motion variables for a given rudder execute and propeller RPM.

Figure 20 shows the simulations results of the turning circle maneuvers with rudder deflection of -35 degrees by using the maneuvering derivatives in Table 8. The starboard turning trajectory, roll angle, and relationship between rudder and heading angle obtained from the FRMT [22] are also presented for the comparison. It is seen that the numerical turning trajectory is adapted to the experimental result. The rate of turn is decreased that results in the larger turning circle in comparison with the turning circle in deep water case. In case of the roll, the roll angle obtained from the current CFD is in good agreement with the estimated roll in the FRMT. It is demonstrated that the ship advance and tactical diameter are well predicted in current CFD-based maneuvering study of the container ship.
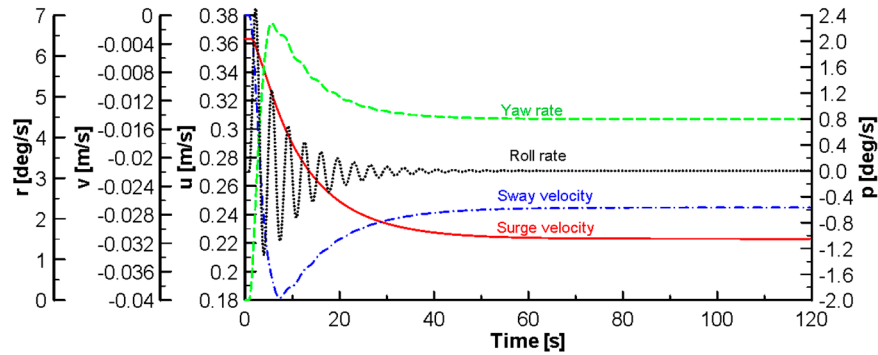
(**a**) Time histories of roll rate, yaw rate, sway velocity and surge velocity
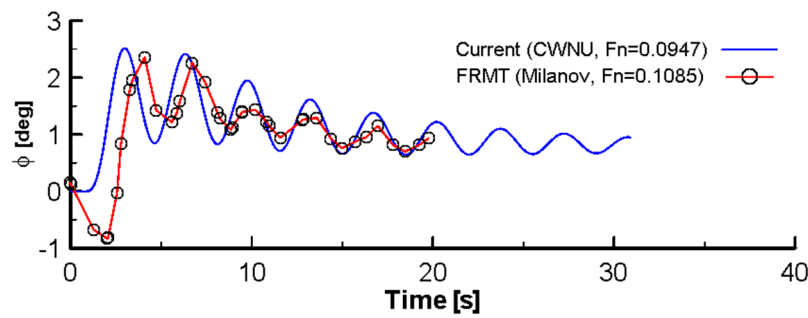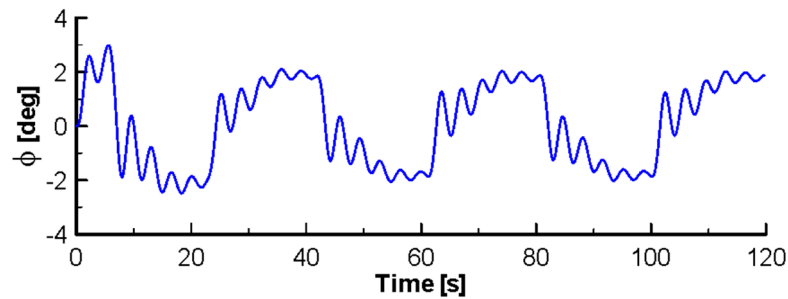

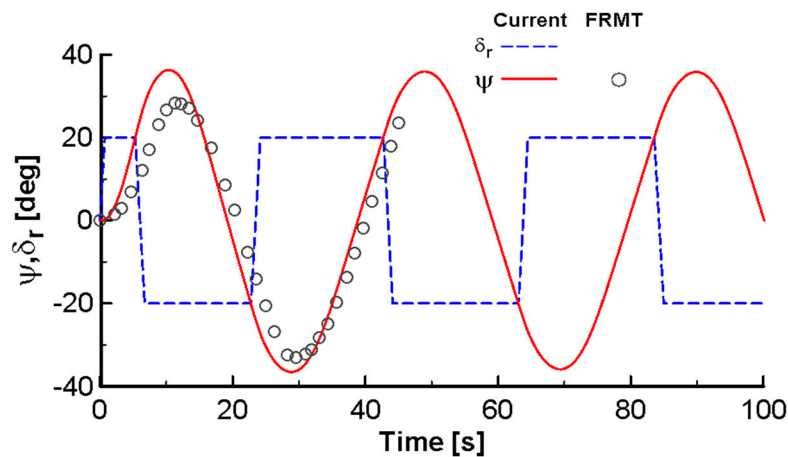(**b**) Time history of roll angle
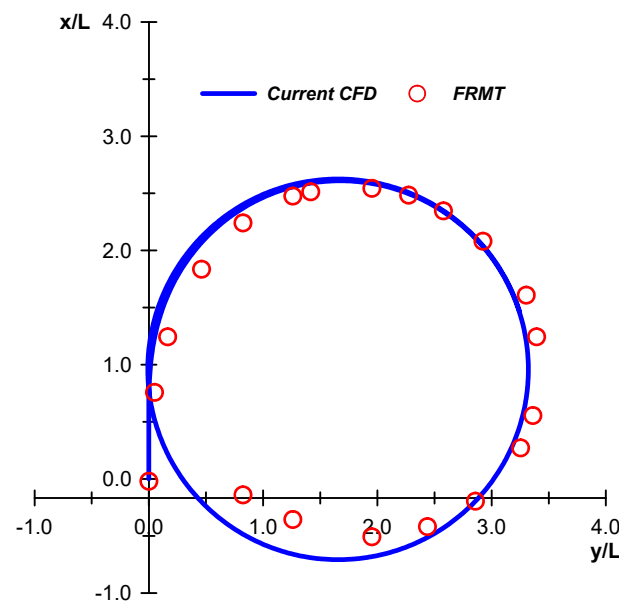
(**c**) Turning trajectory

Figure 21. Turning circle of KCS model circle towards the starboard in comparision with the results of FRMT [22], δ_R = -35°, h/T = 2.0.

(**a**) Time histories of roll rate, yaw rate, sway velocity and surge velocity

(**b**) Time history of roll angle

(**c**) Zigzag path of the ship

Figure 22. Results of 20/20 zigzag test in comparison with the results of FRMT [22], h/T = 2.0.

5. Conclusions

The need for maneuverability of ship in shallow water increases due to the increase of ship size in recent years that calls for the evaluation of maneuvering prediction methods. CFD-based computation is one of the efficient method, which can compromise between the accuracy and high-cost performance in the preliminary design of the ship. Therefore, the dependence of the CFD-based results on the mesh density is analyzed and the 4-DOF maneuverability of the container ship in shallow water conditions is analyzed through the CFD-based estimation of the maneuvering derivatives. All the CFD-based analyses are implemented for the incompressible flow around the bare hull by using the RANS solver in Ansys Fluent code.

The CFD RANS-based simulation of the static drift tests, static heel tests, steady circular tests, and the combined tests are then carried out to estimate the hydrodynamic forces and moments acting on the KCS model. The roll damping and added roll moment of inertia are obatained from the virtual pure roll test. The maneuvering derivatives are derived from the results of the tests by using the

Taylor series. These are introduced to the maneuvering mathematical model of the ship with 4-DOF for evaluating the maneuvering characteristics in shallow water conditions. In general, the predicted derivatives are in good agreement with the experimental data. The KCS maneuvering characteristics obtained from the current CFD-based maneuvering study comply with the results of Free Running Model Tests.

Institutional Review Board Statement

Not applicable.

References

1. Chen, J.; Zou, Z.J.; Xi, C.; Li, X.; Lu, Z. CFD-based simulation of the flow around a ship in turning motion at low speed. *J. Mar. Sci. Technol* **2017**, *Volume 22*, 4, pp. 784-796.
2. Fukui, Y.; Yokota, H.; Yano, H.; Kondo, M.; Nakano, T.; Yoshimura, Y. 4-DOF Mathematical model for manoeuvring simulation including roll motion. *J. Soc. Nav. Archit. Korea.* **2016**, *Volume 24*, pp. 167-179.
3. Gu, H.; Zou, Z. System-based investigation on 4-DOF ship maneuvering with hydrodynamic derivatives determined by RANS simulation of captive model tests. *Appl. Ocean Res* **2018**, *Volume 68*, pp. 11-25.
4. He, S.; Kellett, P.; Yuan, Z.; Incecik, A.; Turan, O.; Boulougouris, E. Manoeuvring prediction based on CFD generated derivatives. *J. Hydrodyn.* **2016**, *Volume 28*, pp. 284-292.
5. Jachowski, J. Assessment of Ship Squat in Shallow Water using CFD. *Arch. Civ. Mech. Eng.* **2008**, *Volume 8*, pp. 27-35.
6. Kim, Y.G.; Yeo, D.; Namsun, S.; Kim, S.; Yun, K.; Oh, B. Prediction maneuverability of KCS with 4 degrees of freedom. *J. Soc. Nav. Archit. Korea.* **2011**, *Volume 48*, pp. 267-274.
7. Menter, F. R. Two-Equation Eddy-Viscosity Turbulence Models for Engineering Applications. *AIAA J.* **1994**, *Volume 32*, pp. 1598-1605.
8. Patel, P.K.; Premchand, M. Numerical Investigation of the Influence of Water Depth on Ship Resistance. *J. Comput. Appl.* **2015**, *Volume 116*, pp. 11-17.
9. Terziev, M.; Tezdogan, T.; Oguz, E.; Gourlay, T.; Demirel, Y.K.; Incecik, A. Numerical investigation of the behaviour and performance of ships advancing through restricted shallow waters. *J. Fluids Struct.* **2018**, *Volume 76*, pp. 185-215.
10. Tezdogan, T.; Demirel, Y.K.; Kellett, P.; Khorasanchi, M.; Incecik, A.; Turan, O. Full-scale unsteady RANS CFD simulations of ship behaviour and performance in head seas due to slow steaming. *Ocean Eng.* **2015**, *Volume 97*, pp. 186-206.
11. Shih, T.H.; Liou, W.W; Shabbir, A.; Yang, Y. and Zhu, Y. A New k – Eddy Viscosity Model for High Reynolds Number Turbulent Flows - Model Development and Validation. *Comput. Fluids* **1995**, *Volume 24*, pp. 227–238.
12. Sung, Y.J.; Park, S.H. Prediction of ship manoeuvring performance based on virtual captive model tests. *J. Soc. Nav. Archit. Korea.* **2015**, *Volume 52*, pp. 407-417.
13. Yasukawa, H.; Hirata, N. Maneuverability and hydrodynamic derivatives of ships traveling in heeled condition. *JASNAOE* **2013**, *Volume 17*, pp. 19-29.
14. Wilcox, D.C., 1988. "Re-assessment of the scale-determining equation for advanced turbulence models", AIAA Journal, Vol. 26, No. 11, pp. 1299-1310.
15. Fossen, T.I. B. Guidance and Control of Ocean Vehicles. Chichester; New York: Wiley, 1994.
16. Piquet, J. Turbulent Flows: Models and Physics. Springer Science & Business Media, 2013.
17. IMO standard for ship manoeuvrability: ANNEX 6.
18. Delefortrie, G.; Eloot, K.; Lataire, E.; VanHoydonck, W.; Vantorre, M. Captive model tests bases 6DOF shallow water model. In Proceedings of 4th MASHCON Conference, Hamburg, Germany, 23-25 May 2016.

19. Eloot, K.; Vantorre; M., 2011. Ship behaviour in shallow water and confined water: an overview of hydrodynamic effects through EFD. In Proceedings of 2nd International Conference on Ship Manoeuvring in Shallow and Confined Water. Trondheim, Norway, 18-20 May 2011.

20. Hamid, S.H.; Araki, M.; Umeda, N.; Sano, M.; Yeo, D.J.; Toda, Y.; Carrica, P.M.; Stern, F. CFD, system – based, and EFD preliminary investigation of ONR tumblehome Instability and capsize with evaluation of the mathematical model. In Proceedings of 12th International Ship Stability Workshop, Washington, USA, 12-15 June 2011.

21. Liu, Y.; Zou, Z.J; Zou, L. RANS-based numerical simulation of captive model test in shallow water for the DTC container carrier. In Proceedings of Fourth International Conference on Ship Manoeuvring in Shallow and Confined Water. Hamburg, Germany, 23-25 May 2016.

22. Milanov, E.; Chotukova, V.Y. Roll motion of container ship in shallow water. In Proceedings of International Conference on Ship Manoeuvring in Shallow and Confined Water, Antwerp, Belgium, 13-15 May 2009.

23. Ruiz, M.T.; Caluwé, S. D.; Zwijnsvooorde, T.V.; Delefortrie, G.; Vantorre, M. Wave effects in 6DOF on a ship in shallow water. In Proceedings of MARSIM Conference, Newcastle University, United of Kingdom, 8th-11th September 2015.

24. Toxopeus, S.L. Viscous-flow Calculations for KVLCC2 in Deep and Shallow Water. In Proceedings of International Conference on Computational Method in Marine Engineering, Lisbon, Portugal, 28-30 September 2011.

25. Vantorre, M. Review of practical methods for assessing shallow and restricted water effects. In Proceedings ofInternational Conference on Marine Simulation and Ship Maneuverability, Kanazawa, Japan, 25-28 August 2003.

26. Gronarz, A. Rechnerische Simulation der Schiffsbewegung beim Manövrieren unter besonderer Berücksichtigung der Abhängigkeit von der Wassertiefe. PhD-Thesis, Unversity of Duisburg, September 11, 1997.

27. Mucha, P. On simulation-based ship maneuvering prediction in deep and shallow water. University of Duis-burg-Essen, Ph.D. thesis, Januart 9, 2017.

28. Bakker, A. Applied Computational Fluid Dynamics. Retrieved from http://www.bakker.org/dartmouth06/engs150/11-bl.pdf.

29. Blancas, F.E.; Roache, P.J. An evaluation of the GCI for unstructured grids. Retrieved from https://cstools.asme.org.

30. International Towing Tank Conference (ITTC), 2011. ITTC-Recommended Procedures and Guidelines: Practical Guidelines for Ship CFD Applications.

31. IMO standard for ship manoeuvrability: ANNEX 6.

32. PIANIC, 1992. Capability of ship manoeuvering simulation models for approach channels and fairways in harbours. PIANIC Report No 20.

33. CFD-Online. Turbulence Intensity. Retrieved from CFD-Online. Retrieved from https://www.cfd-online.com/Wiki/Turbulence_intensity.

34. ANSYS Fluent Theory Guide. Retrieved from https://www.afs.enea.it/project/neptunius/docs/fluent/html/th/node297.htm.

35. Saxena, A. Guidelines for Specification of Turbulence at Inflow Boundaries. Retrieved from http://support.esi-cfd.com/esi-users/turb_parameters/.

36. SIMMAN (2020). Workshop on verification and validation of ship manoeuvring simulation methods, Copenhagen, Denmark. Retrieved from https://www.simman2020.kr.